

# Merging exceptional point and quasi-bound state in the continuum in nanophotonic cavities

*Xiao-Jing Du, Xi-Hua Guan, Yue You, Lin Ma, Jun He and Zhong-Jian Yang\**

*Hunan Key Laboratory of Nanophotonics and Devices, School of Physics, Central South University, Changsha 410083, China University, Changsha 410083, China*

[\\*zjyang@csu.edu.cn](mailto:zjyang@csu.edu.cn)

**ABSTRACT:** In conventional eigenvalue analyses of non-Hermitian systems, the coupling of two modes does not lead to the coexistence of an exceptional point (EP) and a quasi-bound state in the continuum (QBIC) at the same spectral position. Here, we theoretically demonstrate that introducing an excitation-phase degree of freedom enables the merging of an EP and a QBIC (or even a BIC) in nanophotonic cavities. Using coupled-mode theory, we reveal the underlying mechanism of this phenomenon and further validate it via numerical simulations on practical stacked structures. In the EP–QBIC regime, the mode quality ( $Q$ ) factor can be enhanced by over one order of magnitude. Moreover, we systematically investigate the formation conditions for EP–QBIC states and conventional QBICs. Additionally, introducing an excitation-phase degree of freedom in a pure plasmonic structure allows the  $Q$  factor to increase by over 15 times due to QBIC formation—even breaking through the limit imposed by material loss.

## INTRODUCTION

In recent years, non-Hermitian optical technologies have made significant advances, giving rise to a variety of promising research directions<sup>1-3</sup>. Among them, resonant modes in open cavities typically exhibit temporal decay due to radiative losses, but under specific conditions, the system can support localized states known as bound states in the continuum (BIC)<sup>4-7</sup>. However, in practical applications, achieving effective external coupling typically requires the system to deviate slightly from the ideal BIC condition, thereby inducing quasi-BIC (QBIC) resonances<sup>8-12</sup>. Research has shown that single or multiple resonators can support high quality ( $Q$ ) QBICs through symmetry protection, parameter tuning, or accidental field localization in asymmetric structures<sup>4-6, 11, 13-16</sup>. Meanwhile, exceptional points (EP)—another class of singularities unique to non-Hermitian optical systems—have garnered increasing attention<sup>1, 17, 18</sup>. EP occurs when both the eigenvalues and eigenvectors of two modes simultaneously coalesce. Both BIC and EP exhibit tremendous potential in enhancing light–matter interactions<sup>19-22</sup>, enabling applications in sensing<sup>2, 23-25</sup>, lasing<sup>26-29</sup>, and nonlinear optical control<sup>30-37</sup>.

The coexistence of QBIC and EP in the same structure has been reported in several studies<sup>38-41</sup>. For example, EP and QBIC have been observed in metal grating-based dielectric waveguides<sup>42</sup>, coupled polymer waveguides<sup>43</sup>, isolated dielectric cavities<sup>40, 44</sup>, and metasurfaces with broken mirror symmetry<sup>45</sup>. However, merging QBIC and EP at a single spectral point seems intuitively impossible, and the main reason may be related to the mainstream way of understanding them<sup>40</sup>. In

nanophotonic cavities or periodic structures, the optical response of two coupled modes is often described by a non-Hermitian Hamiltonian model<sup>1, 3, 46-48</sup>. The corresponding eigenfrequencies  $\omega_{\pm}$  are expressed as  $\omega_{\pm} = \frac{\omega_1 + \omega_2}{2} - i\frac{(\gamma_1 + \gamma_2)}{2} \pm \sqrt{\frac{[(\omega_1 - \omega_2) - i(\gamma_1 - \gamma_2)]^2}{4} + \kappa^2}$ , where  $\omega_{1,2}$  denote the angular frequencies of the two coupling modes,  $\gamma_{1,2}$  are their damping coefficients, and  $\kappa$  characterizes their coupling strength. The real part of  $\omega_{\pm}$  corresponds to the oscillation frequency of the system, while the imaginary part represents its decay characteristics. In this model, a QBIC (or ideal BIC) corresponds to an eigenmode with a reduced radiation loss rate (or zero), resulting in an increased  $Q$  factor than the original modes. The condition for EP, which requires the expression inside the square root to be zero, directly conflicts with the requirements for QBIC (or BIC). Recently, Adrià Canós Valero and colleagues demonstrated the merging of EP and BIC<sup>49</sup>. In this study, they first construct two separate BIC cases and then bring them to form an EP by tuning parameters. Although the process is still based on the eigenvalue framework, the modes involved in forming the EP-BIC are no longer the two original ones. Instead, each BIC involves two (or more) original modes. Thus this scheme requires complex parameter design.

In this work, we demonstrate that in a nanophotonic cavity system with two interacting modes, the merged EP-QBIC state can be obtained by simply introducing the excitation phase. Theoretically, the excitation phase can be taken into account by using the coupled mode theory (CMT)<sup>13, 50, 51</sup>. In the CMT, proper excitation phase combining an appropriate coupling strength in a photonic cavity can generate an EP-QBIC state (or even an EP-BIC state). To validate the theoretical proposal, we

designed and numerically simulated a vertical dimer cavity with stacked gold (Au)-silicon (Si) nanorods. Simulation results agree with the CMT theoretical predictions well. Meanwhile, we observed the formation of the EP–QBIC state, whose quality factor exhibits an order-of-magnitude enhancement compared with that of an uncoupled case. Additionally, by introducing the excitation phase in a purely plasmonic system, we found that the  $Q$  value of the QBIC state can even surpass the theoretical limit imposed by the intrinsic material loss, highlighting the potential of this system for manipulating light–matter interactions.

## METHOD

Coupled Mode Theory (CMT)<sup>13, 51</sup> is a commonly used theoretical framework for investigating resonant behaviors in optical microcavities such as microdisks and microrings, as well as waveguide structures. For a typical system shown in Fig. 1(a), the coupling can be described by the following equations

$$\begin{bmatrix} \omega_1 - i\gamma_1 - \omega & k \\ k & \omega_2 - i\gamma_2 - \omega \end{bmatrix} \begin{bmatrix} A_1 \\ A_2 \end{bmatrix} = \begin{bmatrix} \gamma_{C1}E \\ \gamma_{C2}e^{i\theta}E \end{bmatrix}, \quad (1)$$

where,  $\omega_1$  and  $\omega_2$  denote the resonant frequencies of original modes 1 and 2, respectively.  $\gamma_1$  and  $\gamma_2$  represent their corresponding losses. The coupling strength is expressed as  $k = \kappa e^{-i\varphi}$ , where  $\kappa$  is the magnitude of the coupling strength, and  $\varphi$  is the phase delay between the two modes.  $\varphi$  can be given by  $\varphi = \frac{2\pi d}{\lambda}$ , where  $d$  is the distance between the two coupling modes, and  $\lambda$  is the operating wavelength.  $A_1$  and  $A_2$  represent the complex amplitudes of the two coupled modes.  $E$  denotes the incident excitation field, while  $\gamma_{C1}$  and  $\gamma_{C2}$  are the excitation coefficients for modes 1 and 2, respectively.  $\theta$  is the excitation phase delay between the two modes.

Eqs. (1) can be rewritten as

$$(H - \omega I) \begin{bmatrix} A_1 \\ A_2 \end{bmatrix} = \begin{bmatrix} \gamma_{C1} E \\ \gamma_{C2} e^{i\theta} E \end{bmatrix}, \quad (2)$$

where the Hamiltonian is

$$H = \begin{bmatrix} \omega_1 - i\gamma_1 & \kappa \\ \kappa & \omega_2 - i\gamma_2 \end{bmatrix}. \quad (3)$$

Subsequently, one can obtain the amplitudes  $A_1$  and  $A_2$  for each mode as

$$A_1 = \frac{k\gamma_{C2}e^{i\theta}E - \gamma_{C1}E(\omega_2 - i\gamma_2 - \omega)}{k^2 - (\omega_1 - i\gamma_1 - \omega)(\omega_2 - i\gamma_2 - \omega)} \quad (4)$$

$$A_2 = \frac{k\gamma_{C1}E - \gamma_{C2}e^{i\theta}E(\omega_1 - i\gamma_1 - \omega)}{k^2 - (\omega_1 - i\gamma_1 - \omega)(\omega_2 - i\gamma_2 - \omega)} \quad (5)$$

The system's extinction spectrum ( $\sigma_{Ext}$ ) can be calculated through the coupling between the incident field and the total response of the system as <sup>13</sup>

$$\sigma_{Ext} \propto |\gamma_{C1}EA_1 + \gamma_{C2}e^{i\theta}EA_2|^2 \quad (6)$$

## RESULTS AND DISCUSSION

Without loss of generality, Fig. 1(b) shows the extinction spectra of original modes 1 and 2 in CMT, both normalized with respect to mode 2. For the sake of demonstration, the high and low resonant frequencies (loss rates) of the original modes are denoted as  $\omega_H$  ( $\gamma_H$ ) and  $\omega_L$  ( $\gamma_L$ ), respectively. Figure 1(c) illustrates the typical response spectra of the coupled system with different excitation phases  $\theta$ . The coupling phase and strength are fixed at  $\varphi = 2\pi/4$  and  $\kappa = 0.94\gamma_L$ , respectively. The case with the excitation phase  $\theta = 0$  exhibits a Fano-resonance lineshape. This lineshape arises from the coherent interference between the two new eigenmodes, which correspond to two Lorentzian peak shapes, one with a broad ( $Q \approx 2.2$ ) peak and

the other with a narrow ( $Q \approx 125$ ) peak (see Supplementary Fig. S1)<sup>52, 53</sup>. This is analogous to the coherent interference between bright and dark modes in common Fano-resonant nanophotonic systems<sup>41, 54-56</sup>. The QBIC phenomenon with coexisting high- $Q$  and low- $Q$  mode pairs corresponds to the conventional QBIC case (denoted by C-QBIC)<sup>4, 19, 32</sup>.

When the excitation phase is adjusted to  $\theta = 2\pi/4$ , the coupled system exhibits a single-peak, narrow-linewidth resonance characteristic. This result indicates the emergence of two new modes at the same frequency, accompanied by a high- $Q$  resonance ( $Q \approx 125$ ), signifying the formation of an EP-QBIC state. Generally, the coupled system exhibits a transition from C-QBIC to EP-QBIC under phase  $\theta$  tuning, characterized by a spectral evolution from a double-peak structure (or its Fano interference) to a single-peak resonance. Notably, by tuning the inter-mode coupling strength  $k$ , both types of QBICs above (C-QBIC and EP-QBIC) can be further tuned into the ideal BICs (C-BIC and EP-QBIC, see Supplementary Fig. S2). In contrast, for the case of  $\theta = 0$ , no matter how the coupling strength  $k$  and the coupling phase  $\varphi$  are adjusted, the EP-QBIC phenomenon cannot be achieved (see Supplementary Fig. S3).

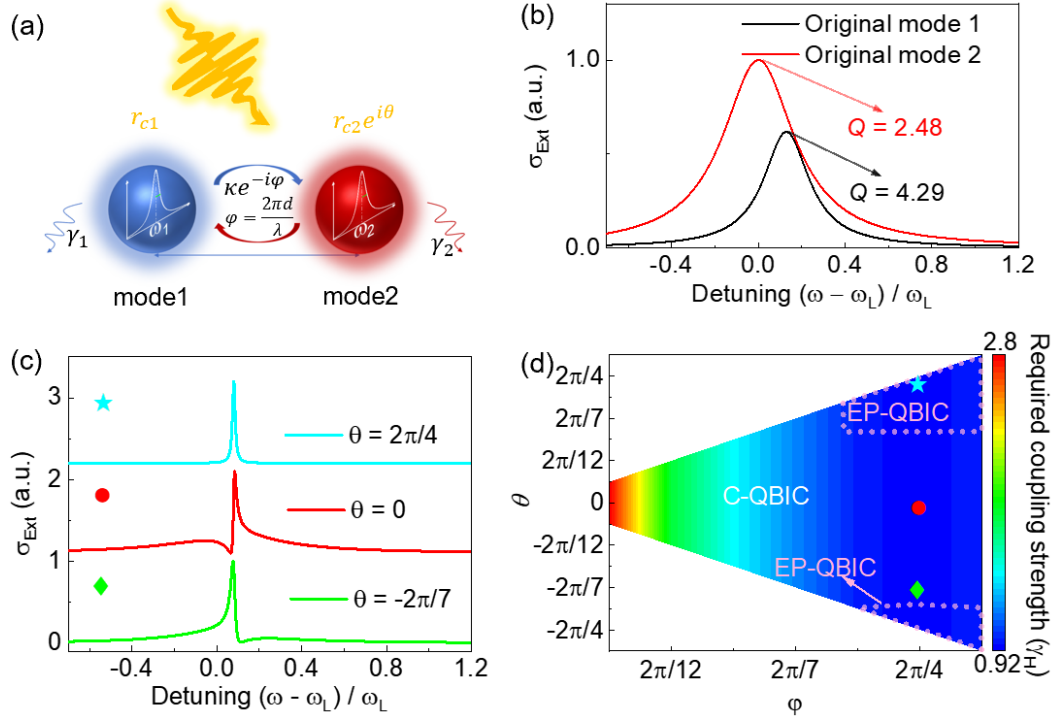


**Figure 1. Two-mode coupled system with EP-QBIC and its spectral characteristics.** (a) Schematic of a two-mode coupled system. The driving field for mode 2 includes an initial phase delay. (b) Normalized extinction spectra of original mode 1 and mode 2. (c) Extinction spectra of the coupled system under different excitation phases  $\theta$ . The coupling phase is  $\varphi = 2\pi/4$ . The coupling strength is  $\kappa = 0.94\gamma_L$ . (d) Mapping of the required coupling strength to achieve QBIC cases as a function of phase parameters  $\theta$  and  $\varphi$ . Here for each QBIC case, the  $Q$  for the higher- $Q$  mode is fixed at  $Q = 125$ . The pentagon, circle, and diamond data points correspond to the spectral conditions shown in panel (c).

Figure 1d quantitatively maps the required coupling strength for realizing QBICs (with a given high  $Q$ -factor of 125) as a function of the phase parameters  $\theta$  and  $\varphi$ . Two distinct regions can be identified. The area outlined by the pink dashed line corresponds to the parameter range for achieving EP-QBIC states, while the region outside this boundary corresponds to the C-QBIC states. In practical nanophotonic systems, the phase delay  $\theta$  induced by plane wave excitation cannot exceed the spatial phase delay  $\varphi$  between two modes, so only the region where  $\theta \leq \varphi$  is

shown. The results reveal that EP–QBICs impose stringent requirements on the parameters, among which an excitation phase delay  $\theta$  is essential. It is worth noting that all the QBICs here correspond to a given high- $Q$  value. If this  $Q$  value is changed, the required coupling strength will vary, but the overall results and discussions remain similar (Fig. S4).

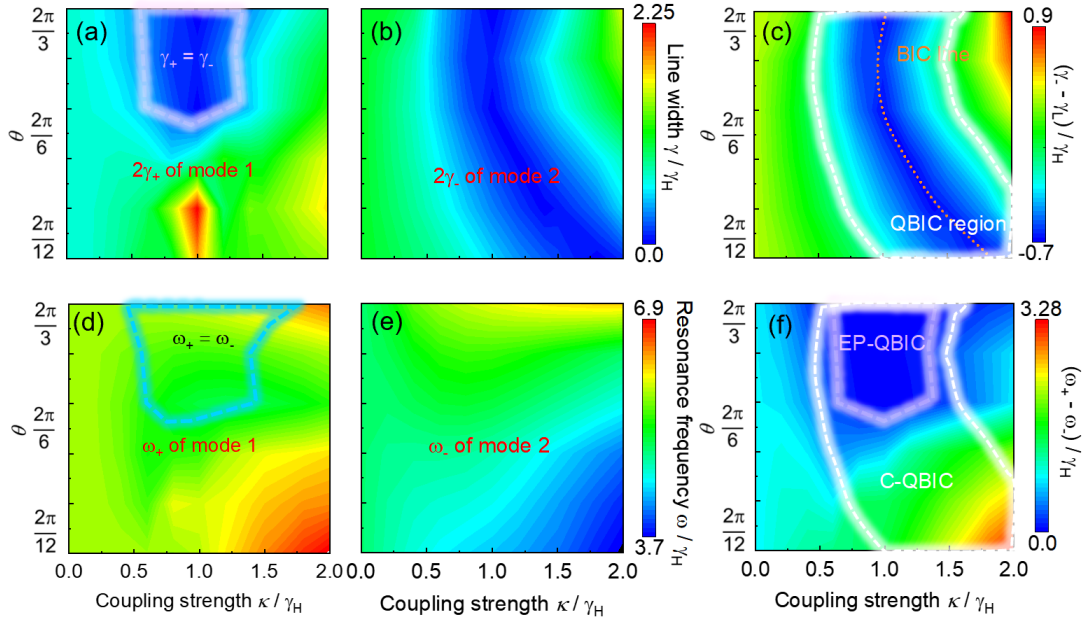


**Figure 2.** EP–QBIC and C–QBIC states with varying the coupling strength  $\kappa$  and phase  $\theta$ . (a, b) Linewidths  $\gamma_+$  and  $\gamma_-$  of the coupled modes. The dashed line shows the region of  $\gamma_+ = \gamma_-$ . (c) Mapping of  $\gamma_- - \gamma_L$ . The dashed white-line area shows the region of  $\gamma_- \leq \gamma_L$ . (d, e) Resonant frequencies  $\omega_+$  and  $\omega_-$  of the coupled modes. The dashed-line area shows the region of  $\omega_+ = \omega_-$ . (f) Frequency differences  $\omega_+ - \omega_-$ . The dashed purple-line area shows the region of EP–QBIC.

To further investigate the formation of EP–QBIC within such a two-mode coupled system, we systematically studied the influence of coupling strength  $\kappa$  and phase  $\theta$  on the optical response of the system.  $\varphi$  is set to be  $\theta = \varphi$  for simplicity, and the original modes involved in the coupling remain the same as those shown in

Fig. 1b. Here, the high and low frequencies of the coupled system are denoted as  $\omega_+$  and  $\omega_-$ , respectively. The corresponding linewidths are denoted as  $\gamma_+$  and  $\gamma_-$ . Figures 2a and 2b show the  $\gamma_+$  and  $\gamma_-$  values of the coupled modes as functions of  $\theta$  and  $\kappa$ . It is seen that  $\gamma_-$  is no larger than  $\gamma_+$  ( $\gamma_- \leq \gamma_+$ ) in this system. Since the formation of a QBIC requires that the linewidth of one coupled mode be smaller than the original low-loss one ( $\gamma_L$ ), we calculated the  $\gamma_- - \gamma_L$  as shown in Fig. 2c. Then, the QBIC region can be easily identified within the area of  $\gamma_- - \gamma_L < 0$  (outlined by the white dashed line). Within this region, there is a special line where  $\gamma_- = 0$ , indicating the emergence of BIC.

The EP situation requires both  $\omega_+ = \omega_-$  (the blue dashed-line region in Fig. 2d.) and  $\gamma_+ = \gamma_-$  (the purple dashed-line region in Fig. 2a). Therefore, their overlapping region defines the EP (the purple dashed-line region in Fig. 2f). The EP region falls entirely within the QBIC domain, indicating the generation of EP–QBIC states. Note that the EP–BIC line (not shown) is also in the EP–QBIC region. The other part within the QBIC region is C–QBIC.

We also considered the effects of loss difference, detuning, and response strength. EP–QBIC states can generally be realized, but their formation depends critically on the parameter  $\theta$ . When  $\theta = 0$ , these states cannot be achieved. In addition, as the ratio of loss difference increases, the coupling strength required to achieve BIC and EP–BIC gradually decreases; a similar trend is observed when the detuning increases (Fig. S5). Note that the reduction of the above required coupling strength does not mean that these cases are easier to realize in practical systems, because these two

cases themselves will also lead to an additional reduction in coupling strength there.

To verify the existence of EP–QBIC states in practical systems, we investigated a configuration based on a vertically stacked Au–Si nanorod dimer (Fig. 3a). Under normal excitation, an excitation phase difference is introduced for the modes of the Si and Au nanorods. The optical responses of the system can be numerically simulated using the finite-difference time-domain (FDTD) method implemented in Ansys Lumerical (see Supplementary Information). Multipole expansion analysis shows that both individual nanorods predominantly support electric dipole modes in the relevant spectral range (Fig. 3b and Fig. S6)<sup>57, 58</sup>. The structural dimensions were chosen to ensure that the resonances of the two original modes are close to each other and the responses are strong, thereby facilitating a relatively large coupling strength.

In the coupled system with a surface gap of 10 nm, the originally detuned resonant modes become degenerate, and their resonance linewidths are significantly narrowed compared to those of the original ones (Figs. 3b and 3c), forming an EP–QBIC mode. The  $Q$ -factor is enhanced by more than an order of magnitude compared to that of the individual nanorods. It is also evident that under the influence of EP–QBIC, the electric field intensity of the Au nanorod is enhanced by more than an order of magnitude compared to the individual Au nanorod (Fig. 3c). Indeed, the excitation phase delay  $\theta$  plays a decisive role in EP–QBIC formation. When the two nanorods are arranged side by side (corresponding to an excitation phase of  $\theta=0$ ), the EP–QBIC effect vanishes entirely (Fig. S8). The crucial role of coupling strength in EP–QBIC can also be highlighted by adjusting the size of the gold nanorods. Reducing

the dimensions of the gold nanorods weakens their plasmonic response (while keeping the phase constant), which in turn causes the EP–QBIC phenomenon to diminish progressively (Fig. S7).

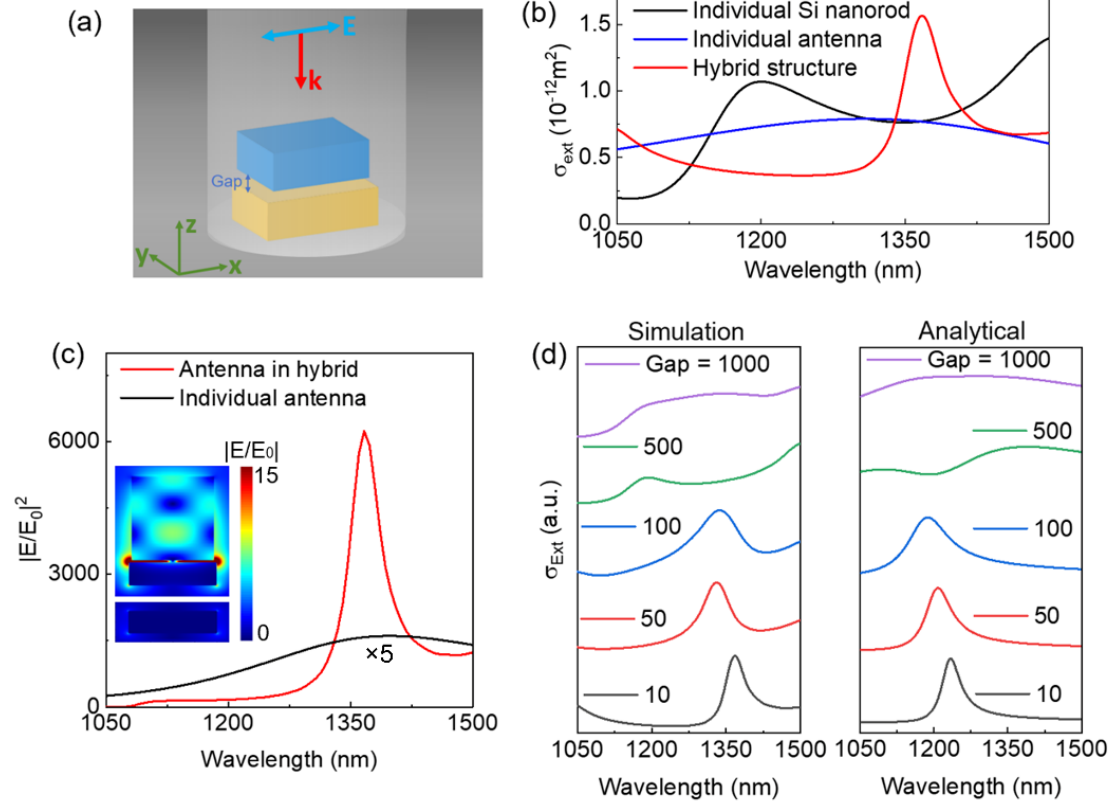


**Figure 3. Generation of EP–QBIC states in practical stacked hybrid cavities.** (a) Schematic of the hybrid dimer system consisting of a Si nanorod and an Au nanorod. The length, width, and height of the Si rod are 340, 230 and 450 nm, respectively. The dimensions of the gold rod are 400, 230 and 150 nm. (b) Simulated extinction spectra of individual Si and Au nanorods as well as the hybrid structure with a surface gap of 10 nm. (c) Simulated field-intensity spectra of the coupled Au nanorod compared to the isolated one. The inset shows their corresponding resonant electric field intensity distributions. (d) Simulated and analytical extinction spectra for the hybrid structure with gap distances varying from 1000 nm to 10 nm. In the analytical model (CMT), the frequency and linewidth of the resonant modes in the Si and Au rods are obtained directly via numerical simulations.  $\omega_{\text{Si}} = 1.0304 \text{ eV}$ ,  $\gamma_{\text{Si}} = 0.2576 \text{ eV}$ ,  $\omega_{\text{Au}} = 0.9512 \text{ eV}$ ,  $\gamma_{\text{Au}} = 0.4394 \text{ eV}$ .  $\gamma_{\text{C1}}$  and  $\gamma_{\text{C2}}$  are also directly extracted from numerical simulations.

To further understand the coupling effects in the coupled system, we varied the gap between the two nanorods in simulations and conducted a comparative analysis based on CMT. All input parameters in the model, except for the coupling strength, are directly extracted from the parameters of the individual modes, including frequency, loss, and phases. A direct mapping relationship exists between the structural parameters (such as nanorod gap dimensions, geometric sizes) and the CMT model coefficients (coupling strength, detuning, and loss). For the case we consider,  $\theta = \varphi$ . As shown in Fig. 3, the analytical results from CMT exhibit good agreement with the simulated results in terms of the trend of linewidth variation. When the distance is below 100 nm, the system can maintain the EP–QBIC states. As the gap distance increases, the single resonance peak (EP–QBIC) gradually splits into two distinct peaks, and the resonance linewidth also broadens accordingly, indicating that EP–QBIC has disappeared. Note that at small gap distances, there is a noticeable deviation in the resonance peak positions between the analytical and simulation results. This discrepancy arises because the plasmon mode of the Au nanorod undergoes a redshift<sup>59</sup> - a well-known phenomenon but not fully accounted for in the current CMT model.

We further investigated a purely plasmonic system composed of two stacked gold nanorods (Fig. 4a) and analyzed it using both numerical simulations and analytical modeling, with the two approaches also showing good agreement. Under appropriate spacing conditions, this system can support the EP–QBIC phenomenon (Fig. 4b). However, the enhancement of the  $Q$  factor is less pronounced than that in Au–Si

hybrid systems, mainly due to the relatively weaker coupling strength. When the inter-rod distance is further reduced (less than  $\sim 50$  nm), the EP-QBIC evolves into the C-QBIC case, with the  $Q$  factor further increasing to 20, even surpassing the theoretical limit ( $\approx 12$ ) imposed by the intrinsic material loss<sup>60,61</sup>. More intriguingly, by tuning the transverse displacement angle  $\varphi$ , the system exhibits a “volcanic eruption”-like spectral line shape. This phenomenon stems from the coexistence of two new modes that share the same resonance frequency but exhibit different loss rates, thus displaying characteristics analogous to a diabolic point (DP)-like state (Fig. 4c and Fig. S9)<sup>44,62,63</sup>.

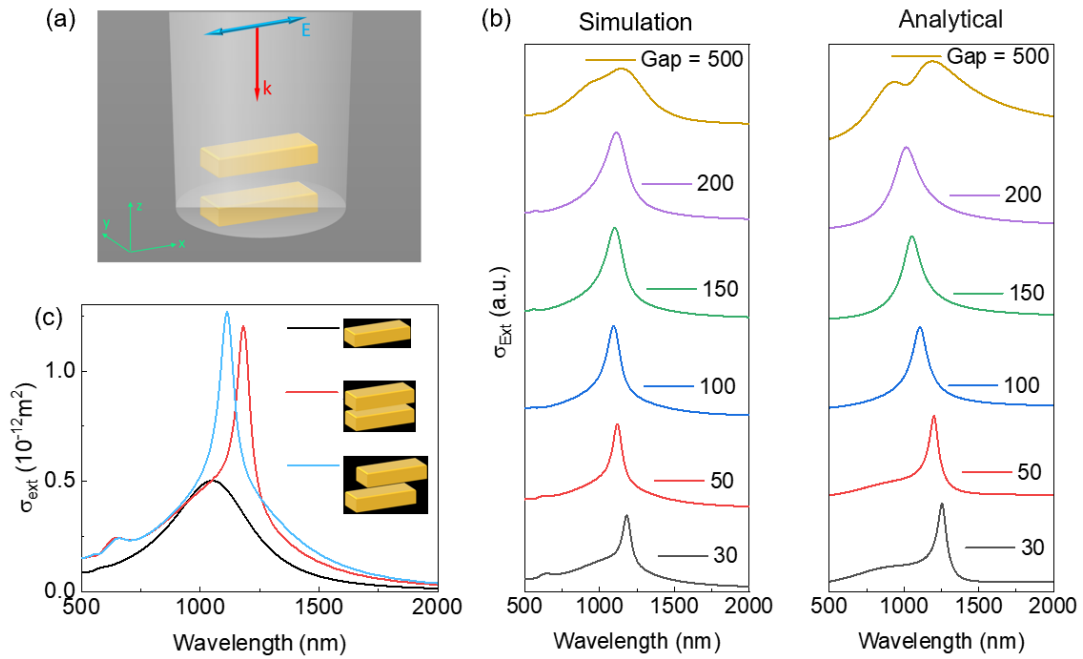


**Figure 4. The case of a pure plasmonic system.** (a) Schematic illustration of a stacked plasmonic nanorod dimer. The two Au nanorods possess identical geometrical dimensions, with a length, width, and height of 308 nm, 120 nm, and 110 nm, respectively. (b) Simulated and analytical extinction spectra for dimers with gap distances varying from 500 to 30 nm. (c) Extinction spectra for a dimer with a gap of 30 nm and the monomer structure. A special case for a dimer with an additional lateral offset of 70 nm is also shown.

Although the analytical model can predict the existence of BICs—including EP–BICs—it remains challenging to approach such states in practical systems. This difficulty primarily arises from the trade-off between the coupling strength and excitation phase. Taking the aforementioned practical systems as an example, achieving a sufficiently strong coupling requires that the participating modes exhibit large enough responses, which can typically be enhanced by increasing the volume. However, in plasmonic structures, once the volume exceeds a certain threshold, further enlargement only broadens the resonance without increasing the intensity near the operating wavelength. For a dielectric cavity system, increasing the volume usually leads to a redshift, so under a fixed operating wavelength, the volume cannot be largely increased. Reducing the distance between the two structures is an effective way to enhance coupling strength, but this also decreases the phase delay, which is an unfavorable factor for generating BICs (Fig. S10 and S12). Of course, this does not imply that BICs cannot be realized in practical nanophotonic cavity systems—it simply means that achieving them within the above practical systems is a great challenge.

## CONCLUSIONS

In this work, we consider the EP–QBIC merged state in a nano-optical cavity system. By employing a CMT model that incorporates external excitation terms, and using the excitation phase as the key tuning parameter for realizing EP–QBIC states. Numerical simulations of a stacked gold–silicon nanorod dimer cavity reveal a clear correspondence between structural parameters (e.g., nanorod gap and geometry) and

CMT coefficients (coupling strength, detuning, and loss), with good agreement between theory and simulation. Guided by this mapping relationship, we achieve synergistic control of the coupling strength and excitation phase by tuning the dimer gap, successfully observing the EP–QBIC merged state and realizing an order-of-magnitude enhancement in the modal  $Q$  factor. Additionally, introducing an excitation-phase degree of freedom in a pure plasmonic structure, the QBIC state can exhibit a  $Q$ -factor exceeding the theoretical limit set by intrinsic material losses. These findings elucidate the underlying physics of EP–QBIC merging and establish a versatile strategy for engineering and controlling such states in tunable non-Hermitian photonic platforms, offering promising opportunities for enhanced light–matter interactions and advanced photonic device applications.

### **Supporting Information**

Supporting Information is available from the Wiley Online Library or from the author.

### **Acknowledgements**

This research was supported by the National Natural Science Foundation of China (11704416), and Innovation and Entrepreneurship Training Program for Students at Central South University (S202410533045).

### **Declaration of competing interest**

The authors have no conflicts to disclose.

### **Data Availability**

Data will be made available on request.

## REFERENCES

- (1) Li, A. D.; Wei, H.; Cotrufo, M.; Chen, W. J.; Mann, S.; Ni, X.; Xu, B. C.; Chen, J. F.; Wang, J.; Fan, S. H.; Qiu, C. W.; Alú, A.; Chen, L. Exceptional points and non-Hermitian photonics at the nanoscale. *Nat. Nanotechnol.* **2023**, *18* (7), 706-720.
- (2) Parto, M.; Leefmans, C.; Williams, J.; Gray, R. M.; Marandi, A. Enhanced sensitivity via non-Hermitian topology. *Light-Sci. Appl.* **2025**, *14* (1), 6.
- (3) Ashida, Y.; Gong, Z. P.; Ueda, M. Non-Hermitian physics. *Adv. Phys.* **2020**, *69* (3), 249-435.
- (4) Rybin, M. V.; Koshelev, K. L.; Sadrieva, Z. F.; Samusev, K. B.; Bogdanov, A. A.; Limonov, M. F.; Kivshar, Y. S. High Q Supercavity Modes in Subwavelength Dielectric Resonators. *Phys. Rev. Lett.* **2017**, *119* (24), 243901.
- (5) Han, S.; Cong, L. Q.; Srivastava, Y. K.; Qiang, B.; Rybin, M.; Kumar, A.; Jain, R.; Lim, W. X.; Achanta, V. C.; Prabhu, S. S.; Wang, Q. J.; Kivshar, Y. S.; Singh, R. All-Dielectric Active Terahertz Photonics Driven by Bound States in the Continuum. *Adv. Mater.* **2019**, *31* (37), 9.
- (6) Huang, L. J.; Xu, L.; Rahmani, M.; Neshev, D.; Miroshnichenko, A. E. Pushing the limit of high Q mode of a single dielectric nanocavity. *Adv. Photonics* **2021**, *3* (1), 016004.
- (7) Huang, L. J.; Xu, L.; Powell, D. A.; Padilla, W. J.; Miroshnichenko, A. E. Resonant leaky modes in all-dielectric metasystems: Fundamentals and applications. *Phys. Rep.-Rev. Sec. Phys. Lett.* **2023**, *1008*, 1-66.
- (8) Rao, X. F.; He, T.; Li, C. F.; Niu, X. S.; Feng, C.; Dong, S. Y.; Zhu, J. Y.; Wei, Z. Y.; Shi, Y. Z.; Qu, J. F.; Wang, Z. S.; Cheng, X. B. Manipulation of resonances governed by Fabry-Perot bound states in the continuum. *Appl. Phys. Rev.* **2025**, *12* (1), 011423.
- (9) Brugnolo, P.; Arslanagic, S.; Jacobsen, R. E. Bound States in the Continuum in Cylindrical All-Dielectric Metasurface Cavities. *Phys. Rev. Lett.* **2025**, *134* (9), 096902.
- (10) Rozman, N.; Fan, K. B.; Padilla, W. J. Symmetry-Broken High-Q Terahertz Quasi-Bound States in the Continuum. *ACS Photonics* **2024**, *11* (5), 1893-1900.
- (11) Liu, S. S.; Huang, S. B.; Zhou, Z. L.; Qian, P.; Jia, B.; Ding, H.; Wang, N. Y.; Li, Y.; Chen, J. Observation of acoustic Friedrich-Wintgen bound state in the continuum with bridging near-field coupling. *Phys. Rev. Appl.* **2023**, *20* (4), 044075.
- (12) Wang, J.; Li, P.; Zhao, X.; Qian, Z.; Wang, X.; Wang, F.; Zhou, X.; Han, D.; Peng, C.; Shi, L.; Zi, J. Optical bound states in the continuum in periodic structures: mechanisms, effects, and applications. *Photon. Insights* **2024**, *3* (1), R01.
- (13) Huang, W.; Liu, S. Y.; Cheng, Y.; Han, J. G.; Yin, S.; Zhang, W. T. Universal coupled theory for metamaterial bound states in the continuum. *New J. Phys.* **2021**, *23* (9), 093017.
- (14) Kalinic, B.; Cesca, T.; Balasa, I. G.; Trevisani, M.; Jacassi, A.; Maier, S. A.; Sapienza, R.; Mattei, G. Quasi-BIC Modes in All-Dielectric Slotted

- Nanoantennas for Enhanced Er<sup>3+</sup>Emission. *ACS Photonics* **2023**, *10* (2), 534-543.
- (15) Koshelev, K.; Lepeshov, S.; Liu, M. K.; Bogdanov, A.; Kivshar, Y. Asymmetric Metasurfaces with High-Q Resonances Governed by Bound States in the Continuum. *Phys. Rev. Lett.* **2018**, *121* (19), 193903.
  - (16) Huang, L. J.; Jin, R.; Zhou, C. B.; Li, G. H.; Xu, L.; Overvig, A.; Deng, F.; Chen, X. S.; Lu, W.; Alu, A.; Miroshnichenko, A. E. Ultrahigh-Q guided mode resonances in an All-dielectric metasurface. *Nat. Commun.* **2023**, *14* (1), 3433.
  - (17) Bulgakov, E.; Pichugin, K.; Sadreev, A. Exceptional points in a dielectric spheroid. *Phys. Rev. A* 2021, *104* (5), 053507.
  - (18) Dong, S.; Wei, H.; Li, Z.; Cao, G.; Xue, K.; Chen, Y.; Qiu, C.-W. Exceptional-point optics with loss engineering. *Photon. Insights* 2025, *4* (1), R02.
  - (19) Kang, M.; Liu, T.; Chan, C. T.; Xiao, M. Applications of bound states in the continuum in photonics. *Nat. Rev. Phys.* 2023, *5* (11), 659-678.
  - (20) Lawrence, M.; Xu, N. N.; Zhang, X. Q.; Cong, L. Q.; Han, J. G.; Zhang, W. L.; Zhang, S. Manifestation of PT Symmetry Breaking in Polarization Space with Terahertz Metasurfaces. *Phys. Rev. Lett.* 2014, *113* (9), 093901.
  - (21) Yang, Z. J.; Huang, P. S.; Lin, Y. T.; Qin, H. Y.; Zuniga-Perez, J.; Shi, Y. Z.; Wang, Z. S.; Cheng, X. B.; Tang, M. C.; Han, S. Y.; Kante, B.; Li, B.; Wu, P. C.; Genevet, P.; Song, Q. H. Creating pairs of exceptional points for arbitrary polarization control: asymmetric vectorial wavefront modulation. *Nat. Commun.* 2024, *15* (1), 232.
  - (22) Bai, T. S.; Wang, W. Z.; Zhang, X. R.; Cui, T. J. Exceptional Point in a Microwave Plasmonic Dipole Resonator for Sub-Microliter Solution Sensing. *Adv. Funct. Mater.* 2024, *34* (13), 2312170.
  - (23) Liao, Z.; Peng, X.; Liu, L. L.; Xu, Y. H.; Xu, K. D.; Pan, B. C.; Luo, G. Q.; Liu, Y. M. Microwave Plasmonic Exceptional Points for Enhanced Sensing. *Laser Photon. Rev.* 2023, *17* (11), 2300276.
  - (24) Mao, W. B.; Fu, Z. T.; Li, Y. H.; Li, F.; Yang, L. Exceptional-point-enhanced phase sensing. *Sci. Adv.* 2024, *10* (14), ead15037.
  - (25) Romano, S.; Zito, G.; Torino, S.; Calafiore, G.; Penzo, E.; Coppola, G.; Cabrini, S.; Rendina, I.; Mocella, V. Label-free sensing of ultralow-weight molecules with all-dielectric metasurfaces supporting bound states in the continuum. *Photonics Res.* 2018, *6* (7), 726-733.
  - (26) Hwang, M. S.; Lee, H. C.; Kim, K. H.; Jeong, K. Y.; Kwon, S. H.; Koshelev, K.; Kivshar, Y.; Park, H. G. Ultralow-threshold laser using super-bound states in the continuum. *Nat. Commun.* 2021, *12* (1), 4135.
  - (27) Wu, T. Y.; Cai, Q.; Jahannia, B.; Patil, C.; Ye, J. C.; Ahmadian, M.; Dalir, H.; Heidari, E. Tunable Laser Using Transverse Cavity Surface Emitting Laser Working near Exceptional Point. *ACS Photonics* 2025, *12* (4), 1754-1759.
  - (28) Zhang, J.; Peng, B.; Özdemir, S. K.; Pichler, K.; Krimer, D. O.; Zhao, G. M.; Nori, F.; Liu, Y. X.; Rotter, S.; Yang, L. A phonon laser operating at an exceptional point. *Nat. Photonics* 2018, *12* (8), 479-484.

- (29) Riabov, D.; Gladkov, R.; Pashina, O.; Bogdanov, A.; Makarov, S. Subwavelength Raman Laser Driven by Quasi Bound State in the Continuum. *Laser Photon. Rev.* 2024, 18 (10), 2300829.
- (30) Choi, Y.; Hahn, C.; Yoon, J. W.; Song, S. H.; Berini, P. Extremely broadband, on-chip optical nonreciprocity enabled by mimicking nonlinear anti-adiabatic quantum jumps near exceptional points. *Nat. Commun.* 2017, 8, 14154.
- (31) Carletti, L.; Koshelev, K.; De Angelis, C.; Kivshar, Y. Giant Nonlinear Response at the Nanoscale Driven by Bound States in the Continuum. *Phys. Rev. Lett.* 2018, 121 (3), 033903.
- (32) Koshelev, K.; Tang, Y. T.; Li, K. F.; Choi, D. Y.; Li, G. X.; Kivshar, Y. Nonlinear Metasurfaces Governed by Bound States in the Continuum. *ACS Photonics* 2019, 6 (7), 1639-1644.
- (33) Xu, L.; Kamali, K. Z.; Huang, L. J.; Rahmani, M.; Smirnov, A.; Camacho-Morales, R.; Ma, Y. X.; Zhang, G. Q.; Woolley, M.; Neshev, D.; Miroshnichenko, A. E. Dynamic Nonlinear Image Tuning through Magnetic Dipole Quasi-BIC Ultrathin Resonators. *Adv. Sci.* 2019, 6 (15), 1802119.
- (34) Hu, Z. C.; Bongiovanni, D.; Jukic, D.; Jajtic, E.; Xia, S. Q.; Song, D. H.; Xu, J. J.; Morandotti, R.; Buljan, H.; Chen, Z. G. Nonlinear control of photonic higher-order topological bound states in the continuum. *Light-Sci. Appl.* 2021, 10 (1), 164.
- (35) Bai, K.; Fang, L.; Liu, T. R.; Li, J. Z.; Wan, D. D.; Xiao, M. Nonlinearity-enabled higher-order exceptional singularities with ultra-enhanced signal-to-noise ratio. *Natl. Sci. Rev.* 2023, 10 (7), 9.
- (36) Zheng, X.; Chong, Y. D. Noise Constraints for Nonlinear Exceptional Point Sensing. *Phys. Rev. Lett.* 2025, 134 (13), 133801.
- (37) Zhu, Y. C.; Hou, J. K.; Geng, Q.; Xue, B. Y.; Chen, Y. P.; Chen, X. F.; Ge, L.; Wan, W. J. Storing light near an exceptional point. *Nat. Commun.* 2024, 15 (1), 8101.
- (38) Yang, Y.; Wang, Y. P.; Rao, J. W.; Gui, Y. S.; Yao, B. M.; Lu, W.; Hu, C. M. Unconventional Singularity in Anti-Parity-Time Symmetric Cavity Magnonics. *Phys. Rev. Lett.* 2020, 125 (14), 147202.
- (39) Sakotic, Z.; Stankovic, P.; Bengin, V.; Krasnok, A.; Alú, A.; Jankovic, N. Non-Hermitian Control of Topological Scattering Singularities Emerging from Bound States in the Continuum. *Laser Photon. Rev.* 2023, 17 (6), 2200308.
- (40) Solodovchenko, N. S.; Samusev, K. B.; Limonov, M. F. Quadruplets of exceptional points and bound states in the continuum in dielectric rings. *Phys. Rev. B* 2024, 109 (7), 075131.
- (41) Liang, Y. Y.; Bochkova, E.; Burokur, S. N.; De Lustrac, A.; Benisty, H.; Lupu, A. Engineering of the Fano resonance spectral response with non-Hermitian metasurfaces by navigating between exceptional point and bound states in the continuum conditions. *Opt. Express* 2024, 32 (5), 7158-7170.
- (42) Kikkawa, R.; Nishida, M.; Kadoya, Y. Bound states in the continuum and exceptional points in dielectric waveguide equipped with a metal grating. *New J. Phys.* 2020, 22 (7), 073029.

- (43) Qin, H. Y.; Shi, X. D.; Ou, H. Y. Exceptional points at bound states in the continuum in photonic integrated circuits. *Nanophotonics* 2022, 11 (21), 4909-4917.
- (44) Zhang, F.; Solodovchenko, N. S.; Fan, H. K.; Limonov, M. F.; Song, M. Z.; Kivshar, Y. S.; Bogdanov, A. A. Non-Hermitian singularities in scattering spectra of Mie resonators. *Sci. Adv.* 2025, 11 (8), eadr9183.
- (45) Zhou, Z. L.; Jia, B.; Wang, N. Y.; Wang, X.; Li, Y. Observation of Perfectly-Chiral Exceptional Point via Bound State in the Continuum. *Phys. Rev. Lett.* 2023, 130 (11), 116101.
- (46) Miri, M. A.; Alù, A. Exceptional points in optics and photonics. *Science* 2019, 363 (6422), 42-+.
- (47) Özdemir, S. K.; Rotter, S.; Nori, F.; Yang, L. Parity-time symmetry and exceptional points in photonics. *Nat. Mater.* 2019, 18 (8), 783-798.
- (48) Wang, C. Q.; Fu, Z. T.; Mao, W. B.; Qie, J. R.; Stone, D.; Yang, L. Non-Hermitian optics and photonics: from classical to quantum. *Adv. Opt. Photonics* 2023, 15 (2), 442-523.
- (49) Valero, A. C.; Sztranyovszky, Z.; Muljarov, E. A.; Bogdanov, A.; Weiss, T. Exceptional Bound States in the Continuum. *Phys. Rev. Lett.* 2025, 134 (10), 103802.
- (50) Haus, H. A. *Waves and fields in optoelectronics*. (Prentice Hall, Englewood Cliffs, NJ, 1983).
- (51) Takata, K.; Roberts, N.; Shinya, A.; Notomi, M. Imaginary couplings in non-Hermitian coupled-mode theory: Effects on exceptional points of optical resonators. *Phys. Rev. A* 2022, 105 (1), 013523.
- (52) Liu, S. D.; Fan, J. L.; Wang, W. J.; Chen, J. D.; Chen, Z. H. Resonance Coupling between Molecular Excitons and Nonradiating Anapole Modes in Silicon Nanodisk-J-Aggregate Heterostructures. *ACS Photonics* 2018, 5 (4), 1628-1639.
- (53) Yang, Z. J.; Deng, Y. H.; Yu, Y.; He, J. Magnetic toroidal dipole response in individual all-dielectric nanodisk clusters. *Nanoscale* 2020, 12 (19), 10639-10646.
- (54) Luk'yanchuk, B.; Zheludev, N. I.; Maier, S. A.; Halas, N. J.; Nordlander, P.; Giessen, H.; Chong, C. T. The Fano resonance in plasmonic nanostructures and metamaterials. *Nat. Mater.* 2010, 9 (9), 707-715.
- (55) Limonov, M. F.; Rybin, M. V.; Poddubny, A. N.; Kivshar, Y. S. Fano resonances in photonics. *Nat. Photonics* 2017, 11 (9), 543-554.
- (56) Solodovchenko, N.; Sidorenko, M.; Seidov, T.; Popov, I.; Nenasheva, E.; Samusev, K.; Limonov, M. Cascades of Fano resonances in light scattering by dielectric particles. *Mater. Today* 2022, 60, 69-78.
- (57) Du, X. J.; Tang, X. T.; Xie, B.; Ma, L.; Hu, M. L.; He, J.; Yang, Z. J. Turning whispering-gallery-mode responses through Fano interferences in coupled all-dielectric block-disk cavities. *Opt. Express* 2023, 31 (18), 29380-29391.
- (58) Xie, B.; Ma, L.; You, Y.; Du, X. J.; Hu, M. L.; Tang, X. T.; He, J.; Yang, Z. J. Coherent energy transfers between orthogonal modes of a dielectric cavity bridged by a plasmonic antenna. *J. Phys. D-Appl. Phys.* 2024, 57 (25), 255110.

- (59) Kelly, K. L.; Coronado, E.; Zhao, L. L.; Schatz, G. C. The optical properties of metal nanoparticles: The influence of size, shape, and dielectric environment. *J. Phys. Chem. B* 2003, 107 (3), 668-677.
- (60) Wang, F.; Shen, Y. R. General properties of local plasmons in metal nanostructures. *Phys. Rev. Lett.* 2006, 97 (20), 206806.
- (61) Qiu, H.; You, Y.; Guan, X. H.; Du, X. J.; He, J.; Yang, Z. J. Efficient entanglement between two long-distance quantum emitters mediated by dark-gap-plasmon waveguides. *Phys. Rev. B* 2024, 110 (7), 075432.
- (62) Zhong, Q.; Nelson, S.; Oezdemir, S. K.; El-ganainy, R. Tuning the strength of exceptional points and their transition to diabolic points. *Opt. Lett.* 2025, 50 (15), 4702-4705.
- (63) Berry, M. V.; Wilkinson, M. Diabolical points in the spectra of triangles. *Proc. R. Soc. Lond. Ser. A* 1984, 392 (1802), 15-43.

# Supplementary Material:

## Merging exceptional point and quasi-bound state in the continuum in nanophotonic cavities

*Xiao-Jing Du, Xi-Hua Guan, Yue You, Lin Ma, Jun He and Zhong-Jian Yang\**

*Hunan Key Laboratory of Nanophotonics and Devices, School of Physics, Central South University, Changsha 410083, China University, Changsha 410083, China*  
[\\*zjyang@csu.edu.cn](mailto:*zjyang@csu.edu.cn)

### **I. FDTD Simulations**

In this study, a Total-Field Scattered-Field (TFSF) plane wave propagating along the  $z$ -axis and linearly polarized in the  $x$ -direction was employed as the excitation source (Figs. 3a and 4a). To ensure high spatial resolution in critical regions—particularly within the nanoscale gap—a uniform and finely discretized mesh was applied, with the grid spacing set to  $\Delta x = \Delta y = \Delta z = 1$  nm. Perfectly Matched Layer (PML) boundary conditions were implemented along all three spatial directions ( $x$ ,  $y$ , and  $z$ ) to effectively suppress non-physical reflections. The silicon nanorod was modeled using silicon (Si), which exhibits negligible optical loss and a refractive index of  $n \approx 3.50$  within the target wavelength range. The dispersive refractive index of gold was adopted from experimental data reported in the Palik optical constants handbook<sup>1</sup>. The surrounding medium was approximated as a vacuum.

## II. Two-Oscillator Fano Interference Model

By analyzing the two-oscillator Fano interference model, the response spectrum  $E(\omega) = |e(\omega)|^2$  can be fitted, thus allowing the contributions of two modes to the system coupling to be obtained<sup>2,3</sup>

$$e(\omega) = a_r + \sum_j \frac{b_j \Gamma_j e^{i\phi_j}}{\omega - \omega_j + i\Gamma_j}, \quad (\text{S1})$$

where  $a_r$  is the background amplitude,  $b_j$ ,  $\gamma_j$ ,  $\phi_j$ , and  $\omega_j$  are the amplitude, damping, phase, and resonant energy of the oscillator  $j$  in the resonant state. The two-oscillator model is employed to fit the extinction spectrum, and consistency was obtained for the calculated and fitted spectra, as shown in Fig. S1.

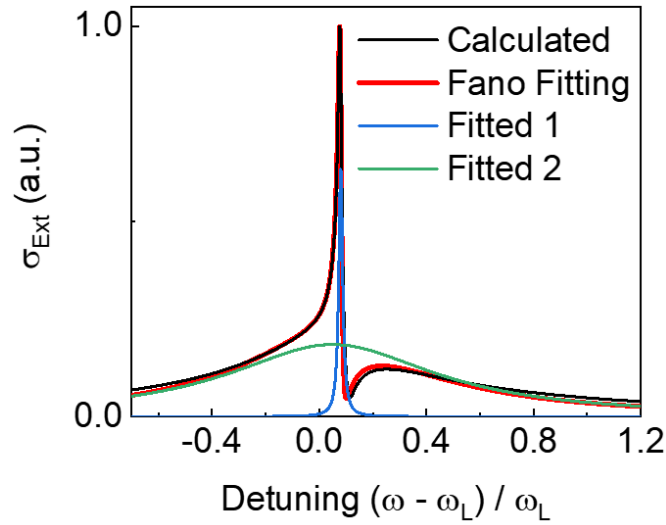


FIG. S1. The directly calculated extinction spectrum based on the CMT model, together with the fitting result obtained using the Fano model. The fitting parameters are  $a_r = 0.01$ ,  $b_1 = 0.796$ ,  $\Gamma_1 = 0.0102$  eV,  $\phi_1 = 1.5708$  rad,  $\omega_1 = 1.2724$  eV;  $b_2 = 0.43$ ,  $\Gamma_2 = 0.556$  eV,  $\phi_2 = 0$  rad,  $\omega_2 = 1.2365$  eV. The blue and green lines represent the two oscillators used in the fitting process.

### III. Different types of QBIC approaching BIC

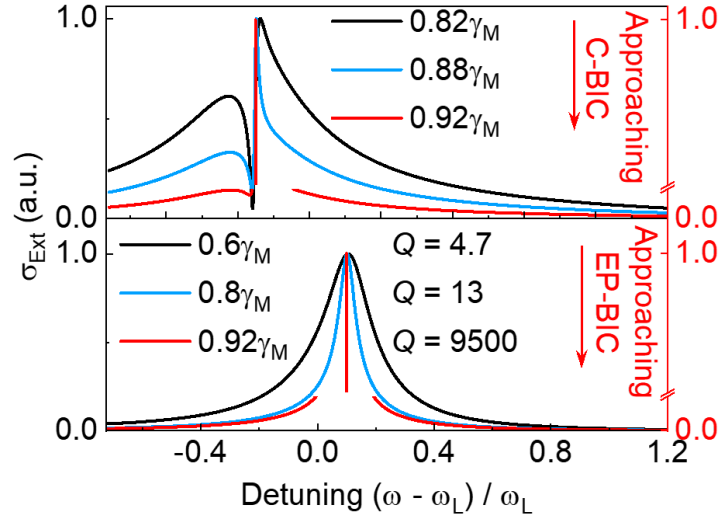


FIG. S2. The upper panel shows the evolution of C-QBIC gradually approaching C-BIC with increasing coupling strength, while the lower panel illustrates the asymptotic convergence of EP-QBIC to EP-BIC as the coupling strength increases. The other parameters are the same as those in Fig. 1c.

### IV. Linewidth and Resonance Frequency of Coupled Modes as Functions of Phase and Coupling Strength at $\theta = 0$

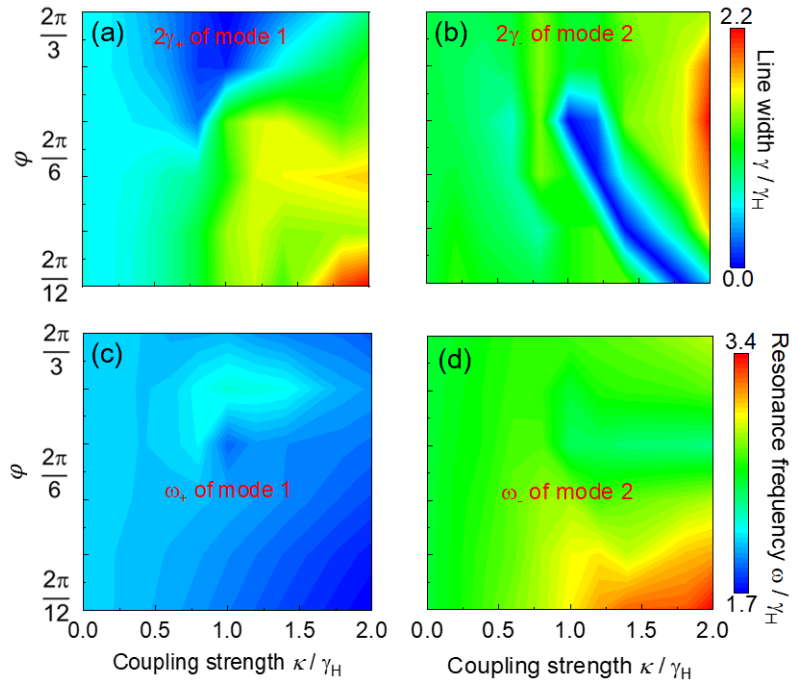


FIG.S3. (a, b) Linewidths  $\gamma_+$  and  $\gamma_-$  of the coupled modes. (c, d) Resonant frequencies  $\omega_+$  and  $\omega_-$  of the coupled modes. The other parameters are the same as those in Fig. 2.

## V. Required coupling strength as a function of phases $\theta$ and $\varphi$ at a fixed quality factor of $Q = 50$

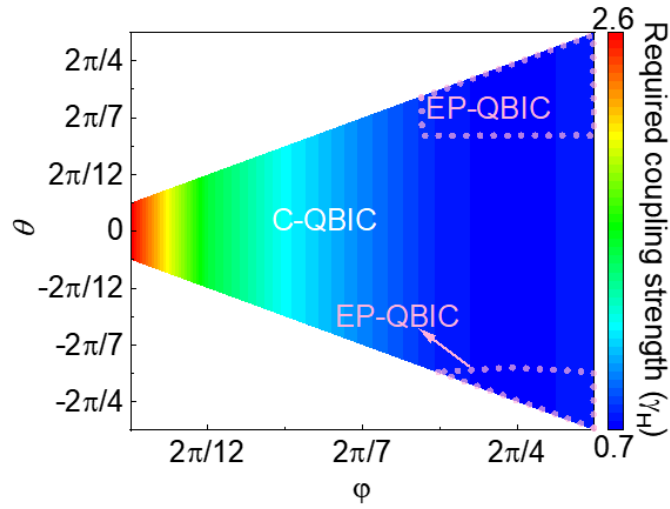


FIG. S4. Mapping of the required coupling strength to achieve QBIC cases as a function of phase parameters  $\theta$  and  $\varphi$ . For each QBIC case, the  $Q$  of the higher- $Q$  mode is fixed at 50. The other parameters are the same as those in Fig. 1d.

## VI. Analysis of Other Parameters for EP-BICs

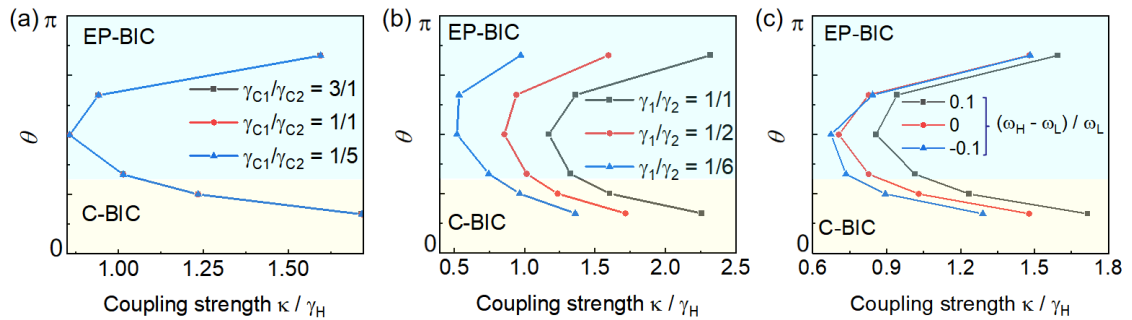


FIG. S5. Required coupling strength  $\kappa$  and phase  $\theta$  for achieving the BIC state under different conditions. For each case,  $\varphi$  is taken to be  $\varphi = \theta$ . (a-d) Results for different excitation coefficient ratios  $\gamma_{C1}/\gamma_{C2}$ , loss rates  $\gamma_1/\gamma_2$ , and detuning  $(\omega_H - \omega_L)/\omega_L$ . The remaining parameters for each case are identical to those in Fig. 1c.

## VII. Full-spectrum and multipole responses of individual Au and Si nanorods

The contributions of different multipole modes to the scattering spectra of Si nanorods and Au nanorods (Fig. 3b) can be calculated using the multipole decomposition method<sup>4, 5</sup>. This approach has been widely employed in micro-nano structures. The spherical analytic expressions with multipolar order  $l$  can be given as

Spherical electric multipole coefficients

$$a_E(l, m) = \frac{(-i)^{l+1}kr}{h_l^{(1)}(kr)E_0[\pi(2l+1)l(l+1)]^{1/2}} \times \int_0^{2\pi} \int_0^\pi Y_{lm}^*(\theta, \varphi) \hat{r} \cdot E_S(r) \sin \theta d\theta d\varphi. \quad (S2)$$

Spherical magnetic multipole coefficients

$$a_M(l, m) = \frac{(-i)^l \eta kr}{h_l^{(1)}(kr)E_0[\pi(2l+1)l(l+1)]^{1/2}} \times \int_0^{2\pi} \int_0^\pi Y_{lm}^*(\theta, \varphi) \hat{r} \cdot H_S(r) \sin \theta d\theta d\varphi. \quad (S3)$$

And the scattering cross-section can be calculated as

$$C_S = \frac{\pi}{k^2} \sum_{l=1}^{\infty} \sum_{m=-l}^l (2l+1) [|a_E(l, m)|^2 + |a_M(l, m)|^2]. \quad (S4)$$

where  $Y_{lm}$  and  $h_l^{(1)}$  represent the scalar spherical harmonics and the spherical Hankel functions of the first kind, respectively. The wave number  $k$  is taken to be that in the surrounding dielectric with impedance  $\eta$ . The scattered electric field  $E_S$  and magnetic field  $H_S$  are obtained from the region surrounding the scatterers using FDTD Solutions. Additionally, the scattering cross-section associated with each spherical multipole order  $l$  can be expressed in terms of basic Cartesian and toroidal multipole

modes of the same order. The  $a_{En}$  (or  $a_{Mn}$ ,  $n = 1, 2, 3 \dots$ ) term corresponds to the multipole order  $n$  of  $a_E(n, m)$  [or  $a_M(n, m)$ ] in the multipole coefficients (Eqs. (S2) and (S3)), where the contributions from all of the  $m$  have been added together for each  $n$ .

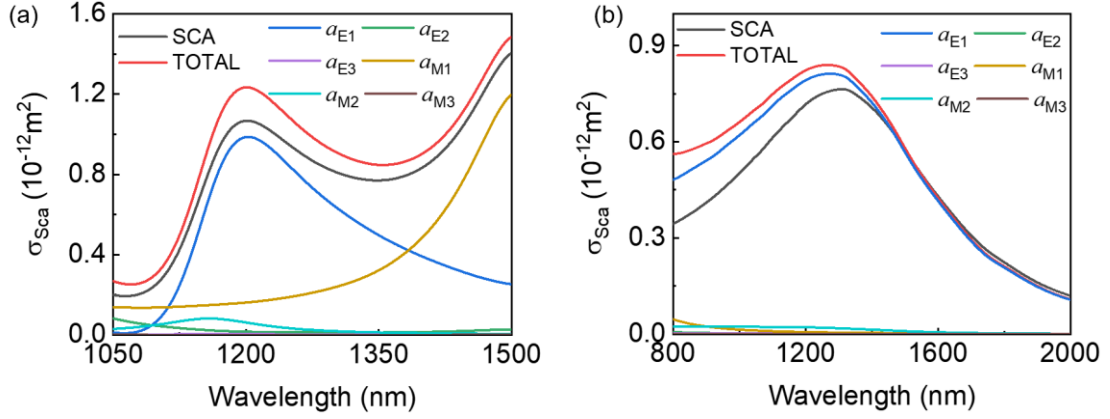


FIG. S6. (a-b) Multipole expansions of the scattering spectra of individual Si and Au nanorods. The parameters of the rods are the same as those in Fig. 3b.

### VIII. Effect of the gold rod size on the EP-QBIC response

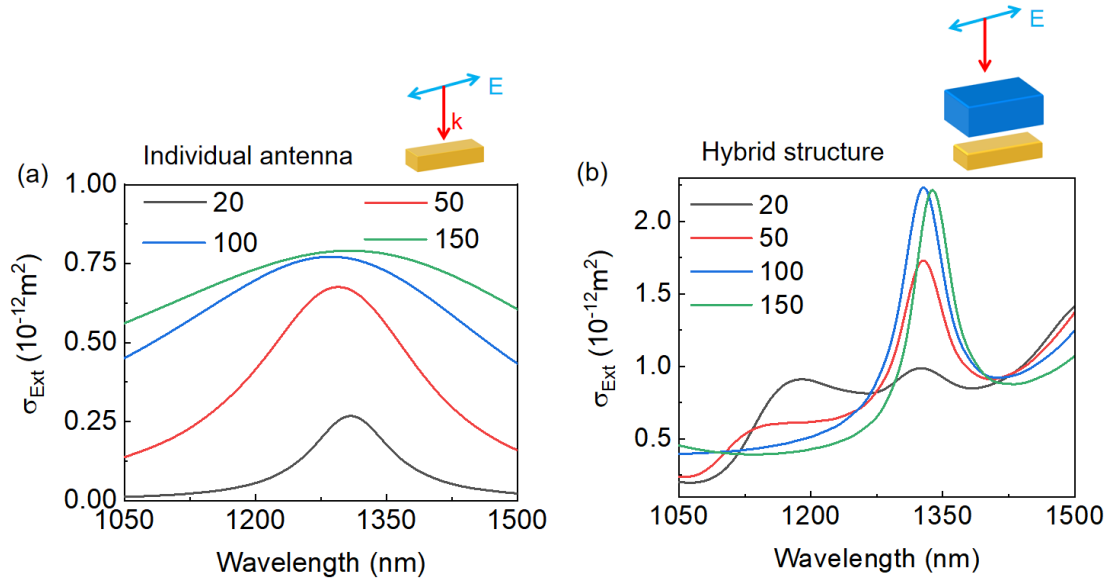


FIG. S7. (a) Extinction spectra of four Au nanorods of different dimensions (length  $\times$  width  $\times$  height).

height):  $240 \times 20 \times 20 \text{ nm}^3$ ,  $370 \times 50 \times 50 \text{ nm}^3$ ,  $400 \times 150 \times 100 \text{ nm}^3$ , and  $400 \times 230 \times 150 \text{ nm}^3$ . (b) Extinction spectra of the hybrid structures formed by pairing each Au nanorod in (a) with a Si nanorod (see Fig. 3b). The center-to-center distance between the nanorods is fixed at 330 nm for all hybrid structure.

### IX. Simulated and analytical results for hybrid structure at excitation phase $\theta = 0$

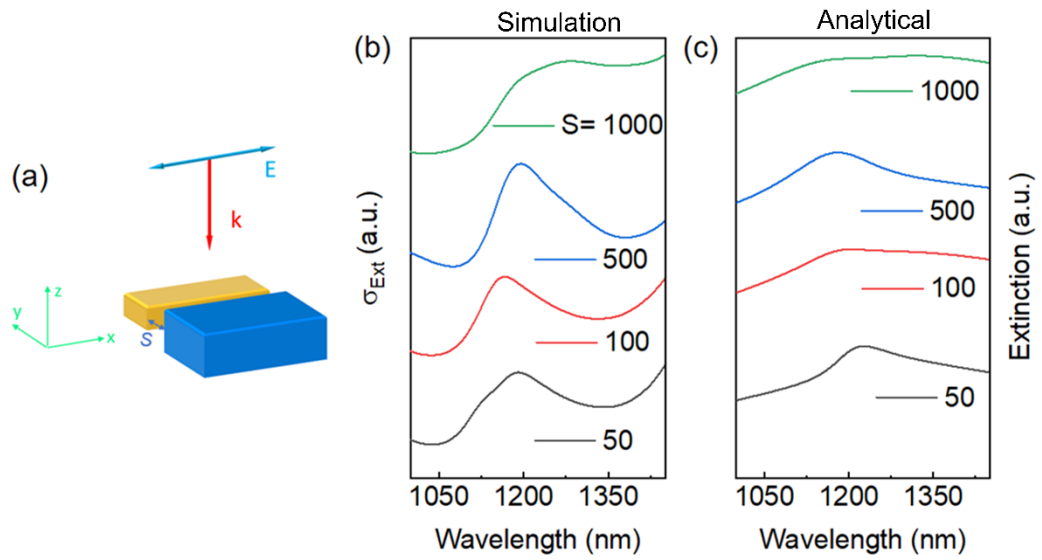


FIG. S8. (a) Schematic diagram of the structure with an excitation phase  $\theta = 0$ . (b, c) Simulated and analytical extinction spectra of the composite structure as a function of separation  $S$ . The parameters of the rods are the same as those in Fig. 3b.

### X. Lorentzian fitting of the “volcano-shaped” spectral profile

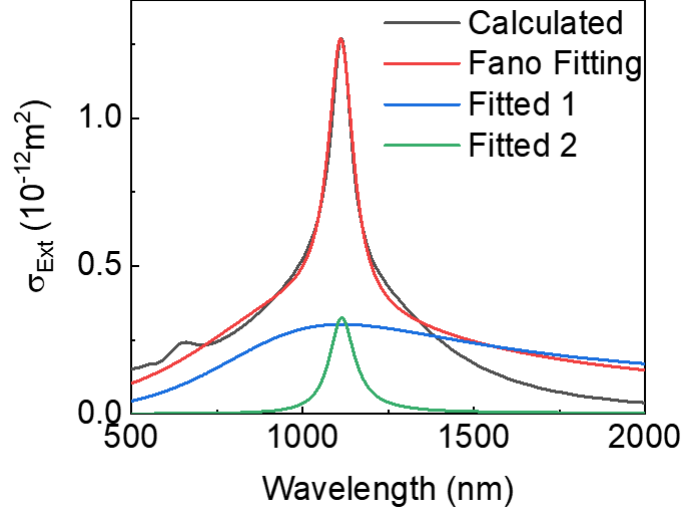


FIG. S9. The extinction spectrum calculated by FDTD and the fitting result obtained using the Fano model. The fitting parameters are  $a_r = 0.1$ ,  $b_1 = 0.55$ ,  $\Gamma_1 = 0.4982$  eV,  $\phi_1 = 0$  rad,  $\omega_1 = 1.1101$  eV;  $b_2 = 0.57$ ,  $\Gamma_2 = 0.0398$  eV,  $\phi_2 = 0$  rad,  $\omega_2 = 1.1101$  eV. The blue and green lines represent the two oscillators used in the fitting process. FDTD simulation results are taken from Fig. 4c, and the fitting method follows the procedure described in Supplementary Section II.

## XI. Paths of the practical systems in their corresponding $\kappa$ - $\theta$ mappings

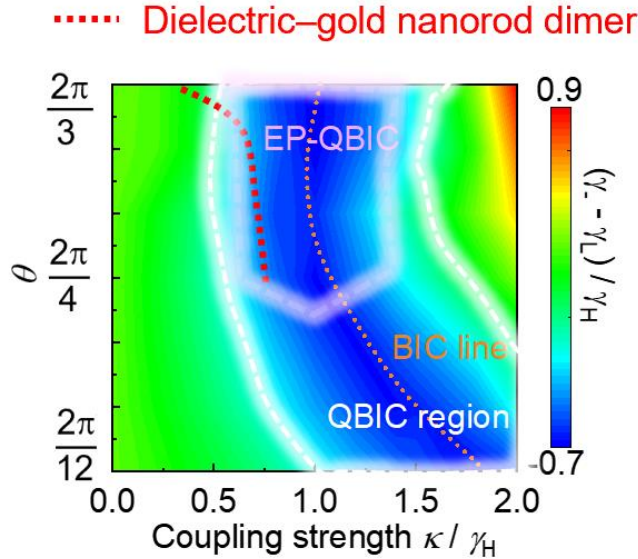


FIG. S10. The analytical results of Fig. 3d (red dashed line) in the corresponding  $\kappa$ - $\theta$  mapping. The  $\kappa$ - $\theta$  mapping is obtained using the same method as in Fig. 2, with parameters taken from Fig. 3d.

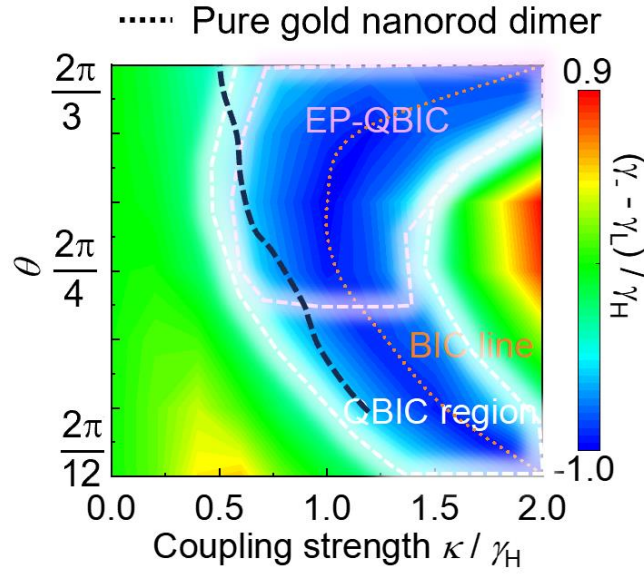


FIG. S11. Analytical results of Fig. 4b (black dashed line) in the corresponding  $\kappa$ - $\theta$  mapping. The  $\kappa$ - $\theta$  mapping is obtained using the same method as in Fig. 2, with parameters taken from Fig. 4d.

## References

- (1) Palik, E. D., *Handbook of optical constants of solids*. Academic press: 1998; Vol. 3.
- (2) Liu, S. D.; Fan, J. L.; Wang, W. J.; Chen, J. D.; Chen, Z. H. Resonance Coupling between Molecular Excitons and Nonradiating Anapole Modes in Silicon Nanodisk-J-Aggregate Heterostructures. *ACS Photonics* **2018**, 5 (4), 1628-1639.
- (3) Yang, Z. J.; Deng, Y. H.; Yu, Y.; He, J. Magnetic toroidal dipole response in individual all-dielectric nanodisk clusters. *Nanoscale* **2020**, 12 (19), 10639-10646.
- (4) Du, X. J.; Tang, X. T.; Xie, B.; Ma, L.; Hu, M. L.; He, J.; Yang, Z. J. Turning whispering-gallery-mode responses through Fano interferences in coupled all-dielectric block-disk cavities. *Opt. Express* **2023**, 31 (18), 29380-29391.
- (5) Xie, B.; Ma, L.; You, Y.; Du, X. J.; Hu, M. L.; Tang, X. T.; He, J.; Yang, Z. J. Coherent energy transfers between orthogonal modes of a dielectric cavity bridged by a plasmonic antenna. *J. Phys. D-Appl. Phys.* **2024**, 57 (25), 255110.